Materials Advances

ROYAL SOCIETY OF CHEMISTRY

PAPER

View Article Online
View Journal | View Issue

Cite this: *Mater. Adv.*, 2026, 7, 3559

Optoelectronic modulation *via* isomerism-induced structural effects in low-dimensional bismuth halide perovskites

Bharath Bhaskarbhat,[a] S. K. Mukaddar,[b] Altaf Pasha,[a] Jan Grzegorz Małecki,[c] Suman Kalyan Sahoo,[a] Srinivas Budagumpi[a] and R Geetha Balakrishna*[a]

The size, functionality and orientation of organic spacer cations in low dimensional perovskites strongly influence their optoelectronic properties. The effect of spacer cation isomerism leads to the formation of distinct ordered perovskites with well-defined structure–property relationships. In this work, the influence of organic spacer isomers—phenylene diammonium (PDA) cations, namely (*o*-PDA)$_2$Bi$_2$I$_{10}$, (*m*-PDA)$_2$Bi$_2$I$_{10}$, and (*p*-PDA)$_2$Bi$_2$I$_{10}$·6H$_2$O, on the optoelectronic behavior of the perovskite-like hybrid organic bismuth halide PDA$_2$Bi$_2$I$_{10}$ is systematically investigated. Structural and electronic variations arising from isomerism are examined using X-ray diffraction, UV-visible absorption spectroscopy, and photoelectron spectroscopy, with further validation provided by density functional theory (DFT) calculations. The PDA cation enables the formation of edge sharing $[Bi_2I_{10}]^{4-}$ dimers, placed close to each other with the I–I distance between adjacent dimers well within the covalent bond requirements. Octahedral dimers are separated by PDA cations, wherein the *ortho* position of the substituent in the spacer cation induces higher strain. Both functional groups interact with the same dimer, causing higher angle distortions and density of states resulting in delocalized electron wavefunctions. The extra advantage of the N contribution to the same dimer in OPDA is that it favours higher absorption and conduction, strongly influencing the optoelectronic properties. Revealing such structure property relationships where weak yet cooperative interactions can still yield macroscopic differences in performance can provide a guide for the design of such low dimensional hybrid organic bismuth halides with desirable properties for functional devices.

Received 4th November 2025,
Accepted 13th February 2026

DOI: 10.1039/d5ma01278c

rsc.li/materials-advances

The emergence of bismuth-based perovskites with structural diversity presents significant potential for lead-free alternatives for optoelectronic devices. These materials have long carrier lifetimes and high absorption coefficients, while also providing improved environmental durability, stability, greater availability, and lower production costs.[1–10] This positions them as promising candidates for sustainable applications, such as in photovoltaics, chemical sensors, electrochemical displays, and light-emitting devices.[11–13]

The coordination geometry of bismuth in hybrid halide perovskites depends on the characteristics of the halogen atom, the charge and size of the organic cation controlling the dimensionality, and the number of hydrogen bond donor sites in the organic moiety.[14–16] $[BiX_6]^{3-}$ octahedra can connect structurally, *via* corners, edges or faces, forming 0D, 1D or 2D structures.[17,18] This structural versatility, coupled with their efficient $s^2 \rightarrow sp$ transitions, enhances their optoelectronic performance.[19–21] The highly rigid $M_2X_9^{3-}$ (M = metal, X = halogen) in bismuth- and antimony-based perovskites can form dimer units in the presence of short organic moieties like methylammonium cations, leading to 0D structures that exhibit strong quantum confinement and dielectric properties.[22–25] However, these dimer units have a 0D structure with insulating organic cations as separators in all directions forming hybrid organic inorganic halobismuthates, often widely referred to as low dimensional perovskites,[26–28] in photovoltaic applications, resulting in poor electronic conductivity. Thus, the selection and versatility of the organic cations provide the ability to tailor the structural and optoelectronic properties of the perovskite, which are intrinsically linked to its dimensionality.[29]

Aromatic cations as organic spacers offer strong prospects attributable to delocalized, conjugated π electron systems and rigid planar structures leading to improved crystallization and dielectric properties.[1] Short diammonium spacers, such as

[a] *Centre for Nano and Material Sciences, JAIN (Deemed –to-be University), Bangalore, Karnataka 562112, India. E-mail: br.geetha@jainuniversity.ac.in*
[b] *Department of Physics, SRM University AP, Amaravati, 522240, Andhra Pradesh, India*
[c] *WSB University, Cieplaka 1c, Dąbrowa Górnicza, Poland*

phenylene diammonium (PDA) cations, allow closer stacking of perovskite layers, enhancing interlayer electronic coupling and charge transport.[30–32] Additionally, the *para* isomer of PDA (*p*-PDA) is reported to improve long-term stability and reduce nonradiative recombination,[33] and has been studied extensively regarding its electronic properties and structural stability.[34–37] Comparing the effects of such isomerism in organic spacers is crucial for fine tuning the optoelectronic behaviour, which remains largely unexplored.

This study involves the creation of a lead free 0D-like perovskite system, $(PDA)_2Bi_2I_{10}$, that possesses a stable quantum-well structure and exhibits improved electronic properties. The effect of the substituent position in the organic spacers, *ortho*-PDA, *meta*-PDA, and *para*-PDA, on the crystallization of this low dimensional perovskite is investigated.

We discuss the structural properties in depth with a focus on the intermolecular interactions that govern the crystal packing. Specifically, crystals with high orientational order of the organic cations positively influence the electronic properties.[38] The reasons for the difference in performance of the *ortho*-isomer in PDA based bismuth perovskite are elucidated through various spectroscopic tools and DFT analysis.[39] We find a difference in the interaction between the spacer and octahedra of these $(PDA)_2Bi_2I_{10}$ 0D-like perovskite systems, correlating well with variations in the packing and disorder of the spacer organic cations. Our results underline that the 0D-like perovskite behaves akin to a molecule, demonstrating that the $(ortho\text{-}PDA)_2Bi_2I_{10}$ isomer has suitable optoelectronic properties for photovoltaic applications. The findings provide helpful guidance for the chemical tuning of substituent positions in spacer cations and reveal the isomerism driven structure–property relationships and optoelectronic properties, showing how weak yet cooperative interactions can still yield macroscopic differences in performance, providing insights into the design of materials with desirable properties for functional devices.

Structural characterization

Solution-processed thin films of bismuth-based low-dimensional perovskites with compositions $(o\text{-}PDA)_2Bi_2I_{10}$, $(m\text{-}PDA)_2Bi_2I_{10}$, and $(p\text{-}PDA)_2Bi_2I_{10}\cdot 6H_2O$ were synthesized (Section S1), and suitable single crystals were obtained (Fig. 1a). These are hereafter termed as OPDA, MPDA, and PPDA, respectively, while their spacer cations are o-PDA, *m*-PDA, and *p*-PDA.

Single-crystal XRD and refinements (CCDC 2433489–2433491) are shown in Table 1b; further parameters and bond lengths are in Tables S1 and S2. OPDA crystallizes in the $P2_1/c$ space group. Octahedral dimers are separated by *o*-PDA cations, linked *via* N–H···I hydrogen bonds (the C–H···I interaction is negligible), forming a 3D-like packing structure (Fig. 1c). The shortest I···I distance between adjacent dimers is 3.79 Å, well below covalent thresholds, indicating compact packing. A $[Bi_2I_{10}]^{4-}$ dimer consists of two $[BiI_6]^{3-}$ octahedra sharing one edge *via* two iodide bridges. The I–Bi–I equatorial angle is 175.80°, the smallest among the analogues, indicating higher strain from *o*-PDA.

MPDA also forms a 0D edge-sharing structure but appears chain-like because one *m*-PDA cation is shared between two dimers in a zig-zag arrangement (Fig. 1c), suggesting pseudo-1D character. It crystallizes in the $P2_1/n$ space group. The shortest I···I distance (3.70 Å) matches its reduced *d*-spacing. MPDA shows the highest asymmetry in bond lengths, 3.099 Å (OPDA 3.088 Å), and the highest distortion index, 0.047 (OPDA 0.040), which enhances polarization and electron wavefunction asymmetry. The Bi–I–Bi inter-octahedral angle deviates the most (93.71°), but the equatorial I–Bi–I angle is relatively high (178.26°), indicating less strain than OPDA and allowing more cation rotation.

PPDA forms a typical 0D edge-sharing perovskite with H_2O molecules in the lattice (Fig. 1c). These interact with the *p*-PDA ammonium group, breaking consecutive dimer connections, and hence reducing stability. The *para*-arranged ammonium group lies out of plane and does not directly interact with the dimer; instead, H_2O bridges the spacer to the dimer *via* ammonium and iodide. PPDA also crystallizes in the $P2_1/n$ space group, has the lowest distortion index (0.037), minimal Bi–I–Bi deviation (88.92°), and the highest equatorial I–Bi–I angle (178.55°), indicating the least strain. Despite compact packing, PPDA crystals are harder to obtain and less stable due to trapped water.

X-ray diffraction spectra for thin films (Fig. 1b) show the first major peaks at low angles: PPDA at 8.65°, MPDA at 8.71°, and OPDA at 9.01°, corresponding to (101) and (011) planes, consistent with SCXRD, confirming low dimensionality. Crystallite sizes (as per Scherrer's equation, and with respect to (011)) reveal that OPDA has the largest average crystallite size (1006 Å) and increased *d*-spacing. This arises from *o*-PDA's *ortho*-NH_3^+ groups, where one cation interacts with only one $[Bi_2I_{10}]^{4-}$ dimer, unlike MPDA and PPDA where one cation links two dimers. This limits rotational freedom, with the other NH_3^+ being either in a void or weakly interacting with the same dimer. Octahedral dimers thus spread asymmetrically and belong to the (011) plane, forming a 0D edge-sharing network. The films were also characterized for elemental composition using EDX, and the results are depicted in Fig. S1. The I^- relative atomic percentage estimated with EDX analysis agrees well with the empirical formula, and no traces of foreign elements were found, satisfying the overall purity of thin films.

In all three isomers, adjacent dimers remain close, with I···I distances under 4.0 Å, allowing them to be described as pseudo-1D. Variations in distortion, rotational freedom, octahedral strain, and packing directly affect the surface electrostatic potential, influencing dipole moment, formation energy, and electron wavefunctions.

Optoelectronic properties

These materials exhibit absorption in the visible region, with optical bandgaps ranging from 2.04 to 2.21 eV, as shown in Fig. 2. These values overlap with the higher end energy bandgap range of 3D perovskites ($FAPbI_3$, $MAPbI_3$). A blue shift is observed in the absorption edge, when *o*-PDA and *m*-PDA are used as spacer cations for $[Bi_2I_{10}]^{4-}$ octahedra in comparison to

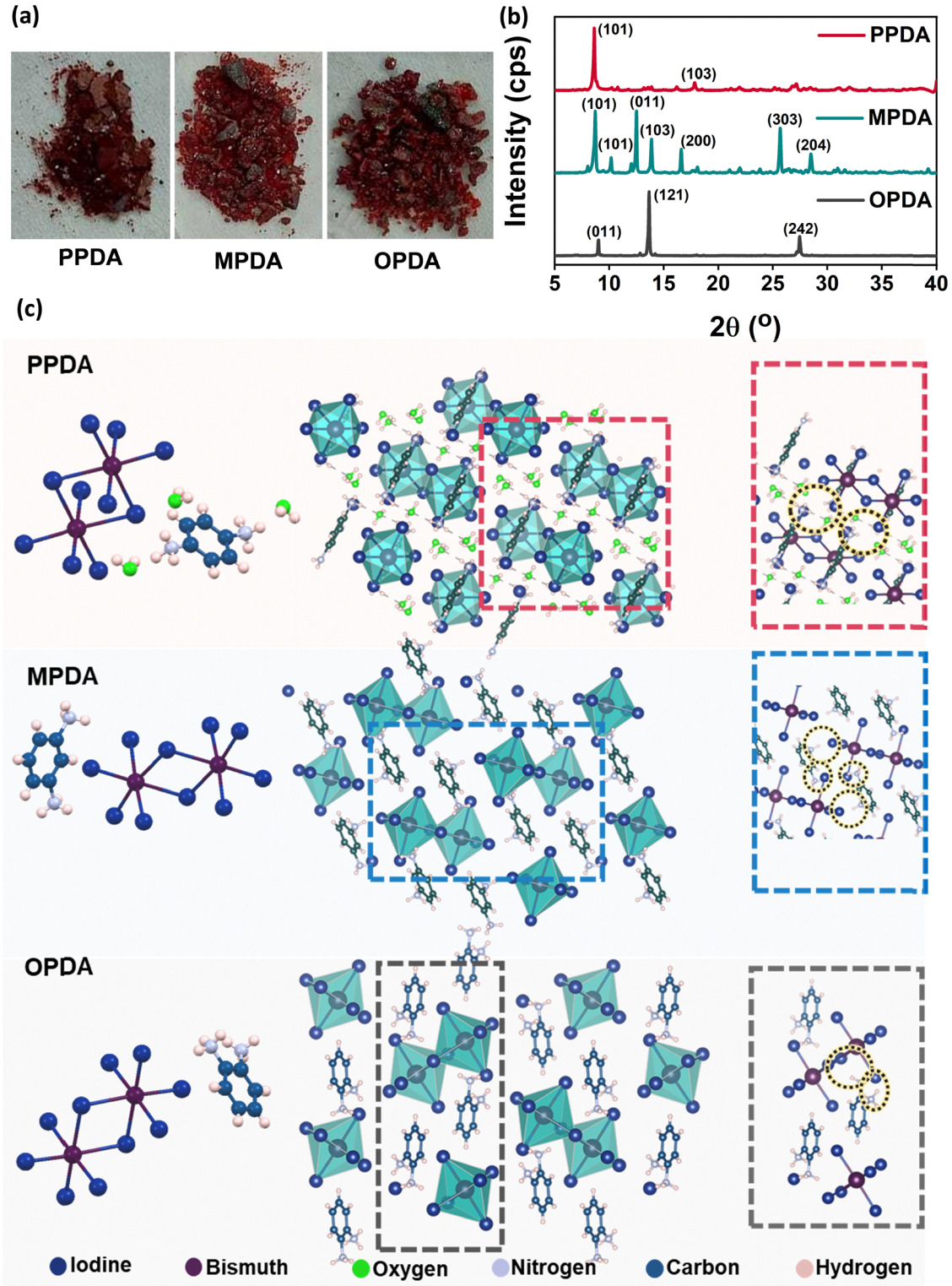

Fig. 1 (a) Digital images of PPDA, MPDA and OPDA single crystals. (b) X-ray diffraction spectra corresponding to thin films of low-dimensional PPDA, MPDA and OPDA perovskites. (c) Schematic illustrations of the crystal packing and molecular structures of the corresponding isomeric PDA-based perovskite-analogues.

p-PDA, and they exhibit optical bandgaps of 2.21 and 2.18 eV, respectively, as seen in Fig. 2a and b. OPDA showed the highest excitonic energy in line with its crystal structure. The fact that PPDA shows a lower bandgap of 2.04 eV compared to MPDA and OPDA can be presumably attributed to a higher equatorial bond angle and shorter bond lengths. An increase in the angle

Table 1 (a) Structural parameters of PPDA, MPDA and OPDA from PXRD analysis. Bond parameters and distortion indices. The distortion index is calculated using $1/6\sum_{1}^{6}[d-D]/D$, where d is the individual bond length and D is the average bond length

(a)

Thin films

Perovskite	Peak position (°)	d-spacing (Å)	FWHM (°)
PPDA	8.65	10.25	0.1232
MPDA	8.71	10.15	0.1414
OPDA	9.01	9.81	0.0827

(b)

Parameter	OPDA	MPDA	PPDA
Bi–I–Bi bond angle (°)	91.51	93.71	88.92
I–Bi–I equatorial bond angle (°)	175.80	178.27	178.55
Bi–I average bond length (Å)	3.088	3.099	3.089
Distortion index	0.042	0.047	0.037

within the octahedra results in a higher degree of overlapping of orbitals in Bi–I octahedra, leading to stronger bonding and antibonding interactions that lower the bandgap. The 6p-orbitals of the bismuth atom contribute more to the conduction band minimum (CBM), whereas the 5p-orbitals of the I atom contribute to both the CBM and valence band maximum (VBM). The band edge observed here not only signifies its origin from transition between I 5p orbitals in the VBM and I 5p and Bi 6p orbitals in the CBM, but also the quantum well octahedral structure. It is important to note that, despite reports by several authors observing emission in 0D[40,41] and 1D[42] perovskites created with aromatic spacers, all of the three isomers showed low visible light emission. The PL maxima are found to be at 540 nm, 572 nm and 565 nm for OPDA, MPDA and PPDA, respectively. OPDA showed a lower Stokes shift of 105 meV, whereas MPDA and PPDA showed photoluminescence at lower energies with Stokes shifts of 241 meV and 244 meV, respectively (Fig. 2b and c). A lower Stokes shift is associated with lower lattice distortion, higher symmetry and weak exciton–phonon coupling.

The electronic structure of these bismuth perovskites was elucidated using ultraviolet photoelectron spectroscopy, as shown in Fig. 3a and b. Though the position of the substituent group (in the spacer) is observed to induce different structural distortion in the perovskites, their electronic signatures closely resembled each other. The electronic band edge calculations are shown in Section S3. The Fermi energy of PPDA with respect to vacuum was found to be at −5.77 eV, while that of MPDA is at −5.76 eV and OPDA at −5.74 eV, as shown in Table 2. The densities of states over energy levels are nearly the same for all three perovskites, ranging from 14.30 eV in OPDA to 14.75 eV in OPDA and 14.92 eV in PPDA.

Valence band maxima with respect to the Fermi energy are shown in Fig. 3b. The spectral weight or photoemission intensity of PPDA and MPDA are higher than that for OPDA because of a higher photoemissive cross section of the crystals and

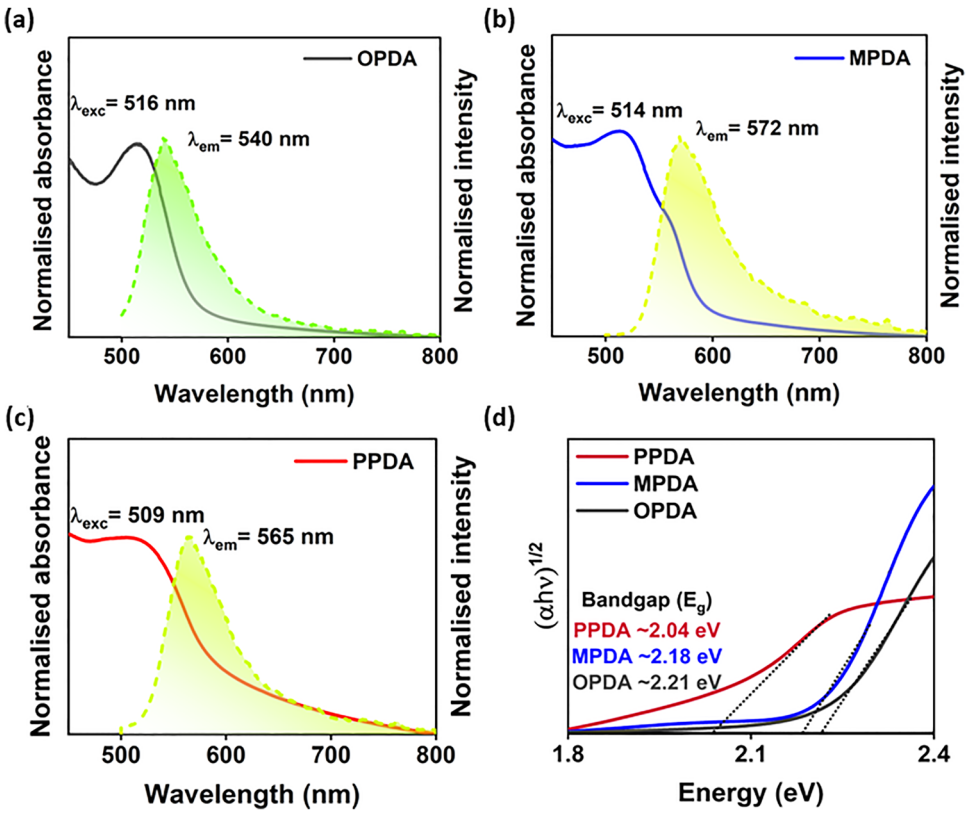

Fig. 2 UV-visible absorption and photoluminescence spectra of (a) OPDA, (b) MPDA and (c) PPDA. (d) Tauc plots of OPDA, MPDA and PPDA.

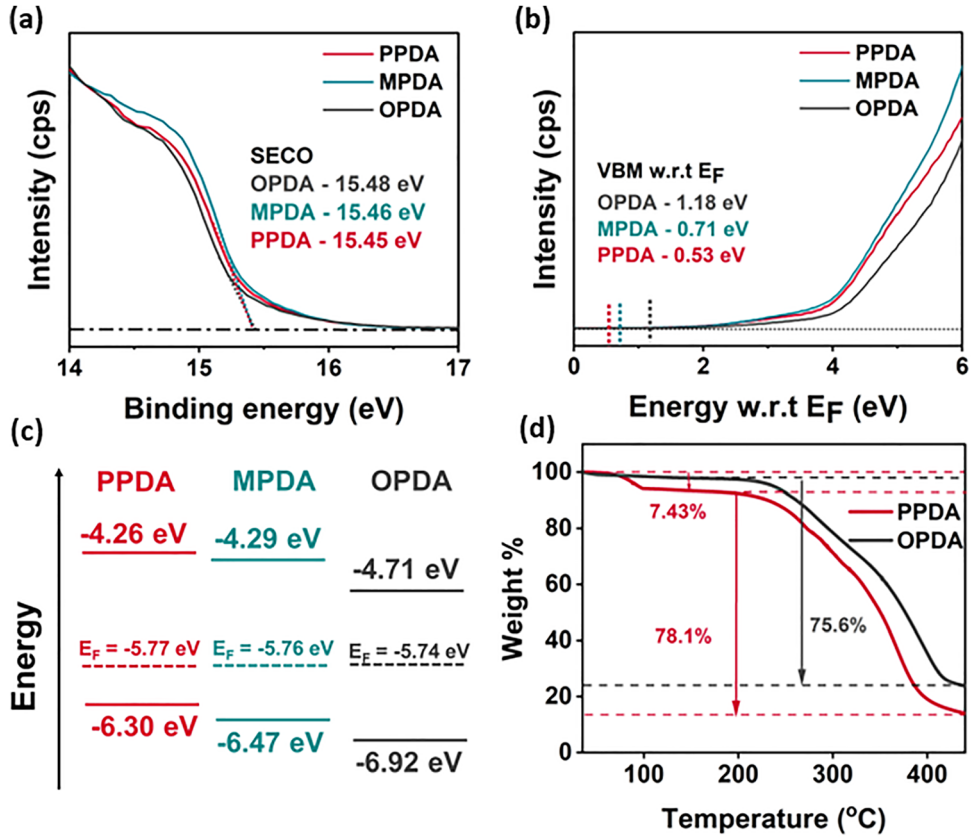

Fig. 3 (a) DOS in the valence band deduced from UPS analysis. (b) VBM w.r.t. E_F. (c) Band alignments of PPDA, MPDA and OPDA. (d) TGA plots of PPDA, MPDA and OPDA compounds.

Table 2 Electronic structure calculations of PPDA, MPDA and OPDA compounds using UPS and UV-visible absorption spectra

Compound	Fermi energy, E_f w.r.t. E_{vac} (eV)	SECO (eV)	VBM (eV)	Bandgap (eV)	CBM (eV)
PPDA	−5.77	15.45	−6.30	2.04	−4.26
MPDA	−5.76	15.46	−6.47	2.18	−4.29
OPDA	−5.74	15.48	−6.92	2.21	−4.71

orbital characteristics and does not imply that OPDA has a lower density of electrons in the available states. The lower the deviation in the bond angles, the more delocalized are the energy levels. OPDA shows a shallower distribution of binding energy due to a higher distortion in the lattice and higher deviation of the bond angle reducing the overlapping of orbitals in the lattice. The equatorial bond angle Bi–I–Bi in PPDA exhibits near-to-ideal geometry, in which the octahedra are intrinsically bent causing less distortion and hence exhibiting a higher distribution of binding energy. MPDA, on the other hand, with a similar equatorial bond angle as PPDA, is seen to have a broader distribution of binding energy, but less than PPDA, presumably due to a greater metal–halide bond length. The Fermi energy levels of these compounds are nearly same (5.75 ± 0.02 eV). The Fermi energy levels of PPDA and MPDA are found to be closer to the VBM of the respective compounds, describing the p-type behaviour of these compounds. PPDA with a nearly ideal inorganic framework shows lower electron affinity compared to MPDA, suggesting that an intrinsically bent metal–halide–metal bond leads to inefficient overlapping of M–X–M orbitals leading to the localization of charge carriers. OPDA exhibits n-type semiconducting nature with a Fermi level aligned at 1.18 eV from the VBM and −1.03 eV from the CBM. The electron affinity in OPDA is found to be the highest among the three owing to a less deviated stretched out metal–halide–metal bond shifting the VBM and CBM deeper than PPDA and MPDA. These studies guide us to determine and rule out energy level mismatches that can happen just by changing the substituent positions in the spacers used for the perovskites. The valence band maximum (VBM) with respect to E_F further shows that the DOS at the VBM is similar for MPDA and PPDA compared to OPDA, suggesting a greater density of electrons in the energy levels induced by the inorganic framework, as illustrated in Fig. 3b. The band alignments of all three compounds are shown in Fig. 3c.

To substantiate the presence of water in the PPDA isomer and to study the thermal stability, thermogravimetric analysis (TGA) was carried out for the PPDA compound and compared with that for the OPDA isomer, as shown in Fig. 3d. The OPDA and PPDA perovskites had good resemblance with each other owing to their same spacer cationic moiety. The decomposition mechanism can be divided into three stages. The first stage is the drying

stage, the second is the decomposition of the spacer cations, and the third stage is the loss of BiI_3. PPDA showed a first significant weight loss of 7.43% in the drying stage, *i.e.* at 71 °C, because of the H_2O molecules present in the unit cell along with *p*-PDA.

This shows that the PPDA has a weaker lattice compared to OPDA, and hence can undergo quick phase transition at a lower temperature. OPDA showed no such loss and proved to be hydrophobic by retaining its initial weight until 233 °C. Decomposition of both the spacer cations is at 230 °C, and hence the first phase transition for OPDA occurs at this temperature. PPDA also shows a phase transition at 235 °C, while the inorganic part is stable until 345 °C and shows a collapse later on. OPDA is stable until 352 °C due to denser crystal packing. The hydrophobic nature of OPDA hence opens possibilities for its use as a passivator for 3D perovskites.

DFT analysis

The band structures of these materials show flat bands suggesting a less dispersive medium as seen in Fig. 4a–c. Comparatively, OPDA shows a little curvature of the bands at the high symmetry point suggesting a higher refractive index medium, making it a more reliable charge carrier than the MPDA and PPDA analogues. Although the bandgaps are in good agreement with the experimental values of 2.14, 2.11 and 2.01 eV for OPDA, MPDA and PPDA, respectively, the deviation in the band alignment from the Fermi energy for OPDA could not be understood. Notably, the valence band maxima and conduction band minima of each phase occur at the same *k*-point, confirming their direct bandgap nature. The total density of states (TDOS) showed remarkable resemblance with the UPS analysis, as depicted in Fig. 4d–f. The I 5p orbitals contribute more near Fermi energy in the valence band, making them a sole contributor to the VBM, whereas bismuth exhibits a fair share of the contribution in defining the conduction band minimum. Surprisingly, OPDA has the extra advantage of nitrogen contribution to the CBM, which is not seen in PPDA, suggesting conduction properties due to ammonium modules of the spacer cation. It also has a higher density of states per eV in both the conduction band and valence band, which is reflected in the higher absorption of light resulting in higher electronic transition as seen in UV-visible spectroscopy. To gain a deeper understanding of the electronic characteristics and the coupling between $[Bi_2I_{10}]^{4-}$ units, we selected representative pairs of Bi_2I_{10} units from each crystal structure and calculated the HOMO and LUMO splitting, following the approach commonly used in molecular organic semiconductors.[43] The HOMO splitting values were found to be 0.12, 0.10, and 0.08 eV for the OPDA, MPDA, and PPDA, respectively, while the LUMO splitting values were 0.09, 0.07, and 0.06 eV. These results indicate moderate electronic coupling between neighbouring $[Bi_2I_{10}]^{4-}$ units, with slightly stronger interactions in the OPDA compared to the MPDA and PPDA. This quantitative assessment complements the band structure analysis and provides deeper insight into the electronic communication pathways in these materials.

The electron localization function provides a deeper insight into the optoelectronic properties of these compounds.

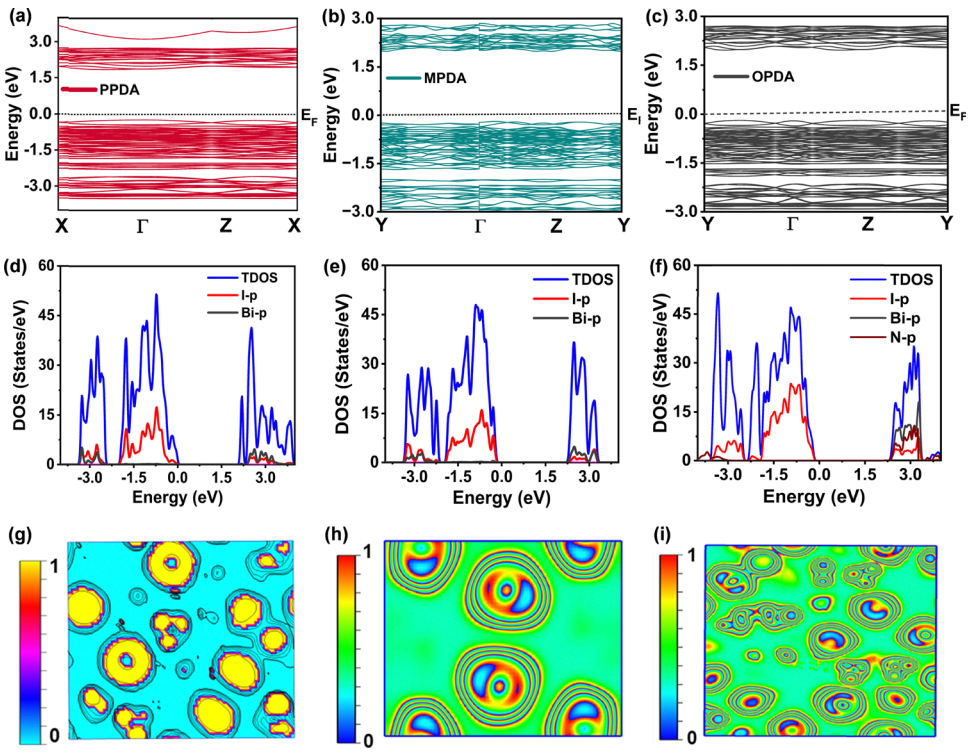

Fig. 4 Band structures of (a) PPDA, (b) MPDA and (c) OPDA. The TDOS of (d) PPDA, (e) MPDA and (f) OPDA. Electron localization functions (ELF) of (g) PPDA, (h) MPDA and (i) OPDA.

Although the optical members are dimers, each octahedron showed the properties of a quantum well individually and not as a dimer. There is greater electron cloud intensity in the cage and prominently on the iodine atoms, proving more localization of electrons in the outer part of the cage as suggested by the TDOS. More interestingly, these 0D structural perovskites are not of the same dimensions electronically. PPDA has intense localization of electrons in Bi–I octahedra and also in H_2O molecules, as seen in Fig. 4g. Other than in these molecules, between the dimers there are no localization and energy levels available for electrons to undergo charge transfer, hindering the mobility between edge shared octahedra. The *p*-PDA spacer cation is not involved in conduction and plays a role of cleaving the octahedral dimers. Electronically, there are 0 degrees of freedom for charge movement making it not suitable for charge transfer, as seen in the TDOS where there is no contribution of I^- near the Fermi energy level.

MPDA, on the other hand, shows prominent localization along the octahedral dimer chain as an electron cloud exists between the dimers. This shows that the potential conductivity in this perovskite is along the octahedral chain, which is structurally confined to 0D but electronically proved to be 1D, spaced by *m*-PDA as seen in Fig. 4h. The fact that the *m*-PDA is not involved in conduction can be attributed to inductive effects or steric hindrance.

OPDA shows interesting properties as the electrons are dominantly localized over the unit cell. This is because unlike the *meta* and *para* isomers, the *ortho* cation contributes to charge delocalization, which makes it suitable for charge conduction as seen in Fig. 4i. The electron cloud in this cation is similar to that of Bi–I octahedra. Interesting properties seen here is the electron localization between the adjacent spacer cations along with more curvature in the energy band diagram compared to MPDA and PPDA, as these are promising for charge transfer between Bi–I–Bi dimers and also between *o*-PDA and Bi–I–Bi dimers. Hence electrons are free to move in all directions making it electronically a 3D perovskite.

In summary, the cation–anion interactions between the isomers of the spacer cation and bismuth iodide octahedra are found to be unique and lead to different arrangements of 0D inorganic networks. The spacer cations significantly influence the I–Bi–I bond parameters in the $[Bi_2I_{10}]^{4-}$ octahedra, which in turn fine-tune the optoelectronic properties. The crystal packing from PXRD of the thin films shows that the OPDA perovskite has a greater *d*-spacing, crystallinity and crystallite size while offering more strain due to greater deviation in the equatorial bond angle but stabilized octahedra compared to MPDA and PPDA, making it suitable for optoelectronic applications. In addition, the lattice parameters of OPDA derived from SCXRD analysis are optimal in comparison with 3D perovskites, and it can be used as a passivator due to its hydrophobic nature, as seen in TGA analysis. Optimal band alignment, higher charge mobility and greater electronic dimensions in OPDA make it more suitable for the discussed applications compared to MPDA and PPDA perovskites. Therefore, optoelectronic properties can be enhanced by the choice of the spacer cation based on the structural properties of different isomers. Additionally, investigation of the substituent effects of different *ortho* isomers on their optoelectronic properties is underway.

Author contributions

Data acquisition, formal analysis, writing – original draft: Bharath Bhaskarbhat, Altaf Pasha, R Geetha Balakrishna. DFT studies – Mukaddar SK, Suman Kalyan Sahoo. SCXRD characterization – John G Malecki. Conceptualization, formal analysis, supervision, funding acquisition, reviewing and editing – R Geetha Balakrishna.

Conflicts of interest

The authors declare no conflict of interest.

Data availability

The data supporting the findings of this study are available within the article and its supplementary information (SI). Additional data are available from the corresponding author on reasonable request. Supplementary information: experimental details, instrumentation, structural parameters, band structure calculations and EDX analysis. See DOI: https://doi.org/10.1039/d5ma01278c.

CCDC 2433489–2433491 contain the supplementary crystallographic data for this paper.[44a–c]

Acknowledgements

The authors are grateful for the support of QuRP, FSID/2024-25/QP/05 and ANRF power fellowship (SPF/2023/000066) funding sources.

References

1 X. Li, J. M. Hoffman and M. G. Kanatzidis, *Chem. Rev.*, 2021, **121**, 2230–2291.
2 M. Leng, Y. Yang, K. Zeng, Z. Chen, Z. Tan, S. Li, J. Li, B. Xu, D. Li and M. P. Hautzinger, *Adv. Funct. Mater.*, 2018, **28**, 1704446.
3 A. Pasha, S. Akhil and R. G. Balakrishna, *J. Mater. Chem. A*, 2021, **9**, 17701–17719.
4 J. K. George, A. Pasha and R. G. Balakrishna, *ACS Appl. Nano Mater.*, 2024, **7**, 19774–19783.
5 S. Akhil and R. G. Balakrishna, *ACS Appl. Energy Mater.*, 2023, **6**, 7487–7496.
6 X. Li, B. Traore, M. Kepenekian, L. Li, C. C. Stoumpos, P. Guo, J. Even, C. Katan and M. G. Kanatzidis, *Chem. Mater.*, 2021, **33**, 6206–6216.
7 L. Duan and A. Uddin, *Mater. Chem. Front.*, 2022, **6**, 400–417.
8 Z. Ma, L. Wang, X. Ji, X. Chen and Z. Shi, *J. Phys. Chem. Lett.*, 2020, **11**, 5517–5530.

9 A. Kaveramma, A. Chakraborty and R. G. Balakrishna, *J. Mater. Chem. A*, 2025, **13**, 3811–3824.
10 S. Akhil, J. Kusuma and R. G. Balakrishna, *J. Cleaner Prod.*, 2022, **366**, 132760.
11 L. Zhang, K. Wang and B. Zou, *ChemSusChem*, 2019, **12**, 1612–1630.
12 G. Li, Y. Zhang, X. Zhao, J. Lin, C. She, S. Liu, C. Jing, Y. Cheng and J. Chu, *Sens. Actuators, B*, 2021, **345**, 130298.
13 A. A. Roselin, N. Anandhan, G. Gopu, I. J. P. Doss, K. Ganesan, R. P. Selvam, T. Marimuthu and G. Sivakumar, *Appl. Phys. A*, 2019, **125**, 1–15.
14 J.-C. Blancon, J. Even, C. C. Stoumpos, M. G. Kanatzidis and A. D. Mohite, *Nat. Nanotechnol.*, 2020, **15**, 969–985.
15 L. Pedesseau, D. Sapori, B. Traore, R. Robles, H.-H. Fang, M. A. Loi, H. Tsai, W. Nie, J.-C. Blancon and A. Neukirch, *ACS Nano*, 2016, **10**, 9776–9786.
16 N. K. Tailor, R. Rohj, K. Dey, S. D. Stranks, D. Sarma and S. Satapathi, *J. Mater. Chem. C*, 2024, 918–927.
17 T. Zhu and X. Gong, *InfoMat*, 2021, **3**, 1039–1069.
18 L.-J. Xu, H. Lin, S. Lee, C. Zhou, M. Worku, M. Chaaban, Q. He, A. Plaviak, X. Lin and B. Chen, *Chem. Mater.*, 2020, **32**, 4692–4698.
19 M. S. Ozório, W. X. Oliveira, J. F. Silveira, A. F. Nogueira and J. L. Da Silva, *Mater. Adv.*, 2020, **1**, 3439–3448.
20 Z. Ma, S. Peng, Y. Wu, X. Fang, X. Chen, X. Jia, K. Zhang, N. Yuan, J. Ding and N. Dai, *Phys. B*, 2017, **526**, 136–142.
21 D. B. Mitzi and P. Brock, *Inorg. Chem.*, 2001, **40**, 2096–2104.
22 Y. Ji, M. She, X. Bai, E. Liu, W. Xue, Z. Zhang, K. Wan, P. Liu, S. Zhang and J. Li, *Adv. Funct. Mater.*, 2022, **32**, 2201721.
23 K. Ahmad, S. N. Ansari, K. Natarajan and S. M. Mobin, *ACS Appl. Energy Mater.*, 2018, **1**, 2405–2409.
24 R. Zhang, X. Mao, Y. Yang, S. Yang, W. Zhao, T. Wumaier, D. Wei, W. Deng and K. Han, *Angew. Chem., Int. Ed.*, 2019, **58**, 2725–2729.
25 J. K. Pious, M. Lekshmi, C. Muthu, R. Rakhi and C. Vijayakumar, *ACS Omega*, 2017, **2**, 5798–5802.
26 J. K. Pious, C. Muthu, S. Dani, A. Saeki and C. Vijayakumar, *Chem. Mater.*, 2020, **32**, 2647–2652.
27 M. I. Saidaminov, J. Almutlaq, S. Sarmah, I. Dursun, A. A. Zhumekenov, R. Begum, J. Pan, N. Cho, O. F. Mohammed and O. M. Bakr, *ACS Energy Lett.*, 2016, **1**, 840–845.
28 J. Yin, P. Maity, M. De Bastiani, I. Dursun, O. M. Bakr, J.-L. Brédas and O. F. Mohammed, *Sci. Adv.*, 2017, **3**, e1701793.
29 E. Mahal, S. C. Mandal and B. Pathak, *Mater. Adv.*, 2022, **3**, 2464–2474.
30 L. Gao, X. Li, B. Traore, Y. Zhang, J. Fang, Y. Han, J. Even, C. Katan, K. Zhao and S. Liu, *J. Am. Chem. Soc.*, 2021, **143**, 12063–12073.
31 P. Fu, M. A. Quintero, C. Welton, X. Li, B. Cucco, M. C. De Siena, J. Even, G. Volonakis, M. Kepenekian and R. Liu, *Chem. Mater.*, 2022, **34**, 9685–9698.
32 Z. Siddique, J. L. Payne, M. T. Sajjad, N. Mica, D. B. Cordes, A. M. Slawin, I. D. Samuel, A. Iqbal and J. T. Irvine, *J. Mater. Chem. C*, 2023, **11**, 223–234.
33 P. Zardari, A. Rostami and H. Shekaari, *Sci. Rep.*, 2020, **10**, 20011.
34 C. Hrizi, A. Samet, Y. Abid, S. Chaabouni, M. Fliyou and A. Koumina, *J. Mol. Struct.*, 2011, **992**, 96–101.
35 C. Hrizi, A. Trigui, Y. Abid, N. Chniba-Boudjada, P. Bordet and S. Chaabouni, *J. Solid State Chem.*, 2011, **184**, 3336–3344.
36 T. Shestimerova, N. Golubev, A. Mironov, M. Bykov and A. Shevelkov, *Russ. Chem. Bull.*, 2018, **67**, 1212–1219.
37 T. A. Shestimerova, N. A. Golubev, M. A. Bykov, A. V. Mironov, S. A. Fateev, A. B. Tarasov, I. Turkevych, Z. Wei, E. V. Dikarev and A. V. Shevelkov, *Molecules*, 2021, **26**, 5712.
38 S. Liu, J. Wang, Z. Hu, Z. Duan, H. Zhang, W. Zhang, R. Guo and F. Xie, *Sci. Rep.*, 2021, **11**, 20433.
39 U. Gunes, F. V. Yaylali, Z. G. Karabag, X.-X. Gao, O. A. Syzgantseva, A. Karabag, G. B. Yildirim, K. Tsoi, N. Shibayama and H. Kanda, *Cell Rep. Phys. Sci.*, 2023, **4**, 101380.
40 D. Cortecchia, J. Yin, A. Petrozza and C. Soci, *J. Mater. Chem. C*, 2019, **7**, 4956–4969.
41 J. Almutlaq, J. Yin, O. F. Mohammed and O. M. Bakr, *J. Phys. Chem. Lett.*, 2018, **9**, 4131–4138.
42 Z. Yuan, C. Zhou, Y. Tian, Y. Shu, J. Messier, J. C. Wang, L. J. Van De Burgt, K. Kountouriotis, Y. Xin and E. Holt, *Nat. Commun.*, 2017, **8**, 14051.
43 Q. Dai, H. Li, G. Sini and J. L. Bredas, *Adv. Funct. Mater.*, 2022, **32**, 2108662.
44 (*a*) CCDC 2433489: Experimental Crystal Structure Determination, 2026, DOI: 10.5517/ccdc.csd.cc2mp7n7; (*b*) CCDC 2433490: Experimental Crystal Structure Determination, 2026, DOI: 10.5517/ccdc.csd.cc2mp7p8; (*c*) CCDC 2433491: Experimental Crystal Structure Determination, 2026, DOI: 10.5517/ccdc.csd.cc2mp7q9.